

ISSN 0029-5515



# nuclear fusion

Nuclear Fusion

Vol 60, No 4

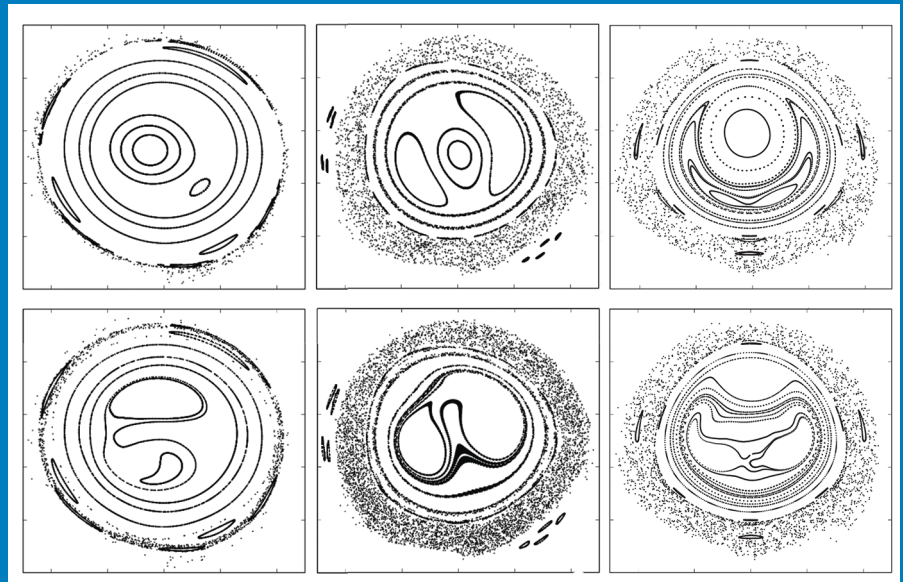
044001-046033

April 2020

Volume 60 Number 4 April 2020

Co-published and edited by the International Atomic Energy Agency  
and IOP Publishing

Online: [iopscience.org/nf](http://iopscience.org/nf)



**IOP** Publishing

International Atomic Energy Agency, Vienna

# Nuclear Fusion

Published monthly by IOP Publishing, Temple Circus, Temple Way, Bristol BS1 6HG, UK and International Atomic Energy Agency, Vienna.  
ISSN: 0029-5515

## Institutional subscription information: 2020 volume

All the prices below include both the printed and on-line versions. Annual subscription: £1374.00. Reduced rate, available to persons whose institutions already subscribe to *Nuclear Fusion*, provided the mailing address is the same as that of the institution: £137.00.

### Orders to:

Journals Subscription Fulfilment  
IOP Publishing  
Temple Circus, Temple Way  
Bristol BS1 6HG, UK

For the USA, Canada and Central and South America, the subscription rate is US\$2305.00 per annual volume. Individual subscription rate: US\$199.00.

### Orders and enquiries to:

IOP Publishing  
PO Box 320  
Congers, NY 10920-0320  
USA

**E-mail:** [ioppublishing@cambeywest.com](mailto:ioppublishing@cambeywest.com)

## Back issues

For prices of back issues and on matters concerning subscriptions, renewals and changes of address, please write to the subscription addresses given above.

**Copyright:** Typographical arrangement © IOP Publishing Ltd. All other content © IAEA unless stated otherwise. Open Access articles are published under a Creative Commons licence, which explicitly states the terms upon which reuse is permitted. No other part of this publication may be reproduced, stored in a retrieval system or transmitted in any form or by any means, electronic, mechanical, photocopying, recording or otherwise, without the prior permission of the relevant copyright holder(s), except as stated below.

Single photocopies of single articles may be made for private study or research, provided that the source is acknowledged.

Multiple copying is permitted in accordance with the terms of licences issued by the Copyright Licensing Agency, the Copyright Clearance Center and other Reproduction Rights Organizations.

**Permission:** Permission to make use of any content other than as set out above may be sought at [permissions@ioppublishing.org](mailto:permissions@ioppublishing.org).

**Moral rights:** Each of the authors of the articles published herein asserts their right to be identified as author of their work in accordance with sections 77 and 78 of the Copyright, Designs and Patents Act 1988.

*Nuclear Fusion* publishes articles making significant advances to the field of controlled thermonuclear fusion. The journal scope includes:

- the production, heating and confinement of high temperature plasmas;
- the physical properties of such plasmas;
- the experimental or theoretical methods of exploring or explaining them;
- fusion reactor physics;
- reactor concepts;
- fusion technologies.

The journal has a dedicated Associate Editor for inertial confinement fusion.

## Editor

A. Fasoli (Switzerland)

## Associate editor for inertial confinement

S. Jacquemot (France)

## Chairman

R. Hawryluk (USA)

## Editorial Board

D. Campbell (UK)	F. Poli (USA)
A.J.H. Donné (EUROfusion)	Y. Sarazin (France)
S. Dudarev (UK)	H. Shiraga (Japan)
T. Estrada (Spain)	W. Solomon (USA)
D. Farina (Italy)	W. Suttrop (Germany)
V. Goncharov (USA)	H. Shiraga (Japan)
Y.-S. Hwang (Republic of Korea)	Y. Ueda (Japan)
K. Ida (Japan)	D. Whyte (USA)
S. Ide (Japan)	R. Wolf (Germany)
S. Ishida (Japan)	E. Wolfrum (Germany)
T. Jones (UK)	G. Xu (China)
T. Kurki-Suonio (Finland)	M. Xu (China)
T. Luce (ITER)	M. Yoshida (Japan)
S. Y. Medvedev (Russian Federation)	G. Zhuang (China)

## Editors emeriti

D. Twersky (Deceased)  
C. Bobeldijk (Deceased)  
D.W. Ignat  
F.C. Schüller  
R.D. Stambaugh  
P. Thomas

## IAEA, Vienna

**Journal Manager** S. Le Masurier

**Editorial Assistants** B. Papadopoulou and D. Yarullina

## IOP Publishing, Bristol

**Publisher** R. Gillan

**Editorial Assistant** S. Poulter

**Production Editor** S. Turner

**Marketing Executive** A. Coombs

## Publishing office

IOP Publishing  
Temple Circus, Temple Way  
Bristol BS1 6HG, UK  
**Tel:** +44 (0)117 929 7481  
**Fax:** +44 (0)117 929 4318  
**E-mail:** [fusion@ioppublishing.org](mailto:fusion@ioppublishing.org)

## Editorial office

International Atomic Energy Agency  
Wagramer Strasse 5, P.O. Box 100  
A-1400 Vienna, Austria  
**Tel:** +43 1 2600 2 6195  
**Fax:** +43 1 2600 2 9655  
**E-mail:** [nf@iaea.org](mailto:nf@iaea.org)

## Front cover picture

Poincaré surfaces of section showing magnetic topology from the simulations. See article 046024 by S. Munaretto *et al* in this issue.

PAPER

## Generation and suppression of runaway electrons in MST tokamak plasmas

To cite this article: S. Munaretto *et al* 2020 *Nucl. Fusion* **60** 046024

View the [article online](#) for updates and enhancements.



**IOP | ebooks™**

Bringing together innovative digital publishing with leading authors from the global scientific community.

Start exploring the collection—download the first chapter of every title for free.

# Generation and suppression of runaway electrons in MST tokamak plasmas

S. Munaretto<sup>1,a</sup>, B.E. Chapman<sup>1</sup>, B.S. Cornille<sup>2</sup>, A.M. DuBois<sup>1,b</sup>,  
K.J. McCollam<sup>1</sup>, C.R. Sovinec<sup>2</sup>, A.F. Almagri<sup>1</sup> and J.A. Goetz<sup>1,c</sup>

<sup>1</sup> Department of Physics, University of Wisconsin-Madison, Madison, WI 53706,  
United States of America

<sup>2</sup> Department of Engineering Physics, University of Wisconsin-Madison, Madison, WI 53706,  
United States of America

E-mail: [munaretto@fusion.gat.com](mailto:munaretto@fusion.gat.com)

Received 13 September 2019, revised 21 December 2019

Accepted for publication 6 February 2020

Published 11 March 2020



## Abstract

This paper explores the behavior of runaway electrons in tokamak plasmas at low electron density, plasma current, and magnetic field using experimental data from the Madison Symmetric Torus (MST) and computational data from the NIMROD nonlinear resistive 3D MHD code. Density thresholds for the onset and suppression of runaway electrons are determined experimentally in steady tokamak plasmas, and in plasmas with a population of runaway electrons, resonant magnetic perturbations with different poloidal mode numbers are applied. Poloidal mode number  $m = 3$  perturbations suppress the runaway electrons, while perturbations with  $m = 1$  have little effect. This difference is consistent with the difference in computed magnetic topologies. The  $m = 1$  RMP has little effect on the topology, while the  $m = 3$  RMP produces a broad region of stochasticity, which can allow for rapid loss of the runaway electrons.

Keywords: runaway electrons, resonant magnetic perturbations, tokamak, MHD

(Some figures may appear in colour only in the online journal)

## 1. Introduction

Runaway electrons are a potential problem for ITER and other future tokamak fusion devices, in particular during disruptions. The toroidal electric field generated during the plasma current quench in a large tokamak can accelerate electrons to well above the thermal speed. For such electrons the collision frequency decreases with increasing velocity, allowing their kinetic energy to increase rapidly. Each of these electrons can, in a single collision, accelerate another thermal electron above the thermal speed, while still remaining above that speed itself. This process leads to an exponential growth of the runaway population. In this two-step process, the electrons

initially accelerated by the current quench are usually referred to as the seed population, and the electrons accelerated later by collisions are referred to as the runaway avalanche [1–7]. With an ultimate energy from 10–100 MeV, avalanche electrons can cause significant damage to plasma-facing components [8].

A number of mitigation strategies for runaway electrons (REs) are being investigated [9]. The one probably best understood, and therefore envisioned for ITER, is enhancement of electron energy loss via Coulomb collisions. The enhancement has been achieved with massive gas and/or shattered pellet injection in present devices like DIII-D [10–12], TEXTOR [13], and K-STAR [14]. But this type of approach presents challenges for ITER, including sufficient assimilation of the injected material by the plasma and stress on the vacuum system, such that it remains uncertain if a sufficient amount of material can be injected. Another possible solution for RE mitigation is the application of a resonant magnetic perturbation (RMP), which is at present not considered a principal strategy

<sup>a</sup> Present address: General Atomics, San Diego, CA 92121, United States of America

<sup>b</sup> Present address: U.S. Naval Research Laboratory, Washington, DC 20375, United States of America

<sup>c</sup> Present address: Department of Engineering Physics, University of Wisconsin-Madison, Madison, WI 53706, United States of America

for ITER but which could ultimately be complementary to the injection of particles. The RMP can introduce stochasticity in the plasma, enhancing electron transport and minimizing the energy that any runaway electrons can achieve. This was shown in ASDEX-Upgrade [15], COMPASS [16] TEXTOR [17, 18], DIII-D [19], JT-60U [20], and RFX-mod [21], and has been investigated in MST reversed-field pinch plasmas [22]. It was also initially predicted for ITER [23, 24], although more recent work suggests that it may not be a viable solution due to a limit on the current that can be driven in the ELM suppression coils [25, 26].

Regardless of the ultimate utility of an RMP for runaway electron mitigation in ITER, RMP physics in general continues to be a widely studied topic worldwide, and application and diagnosis of an RMP on present devices presents a powerful, controlled means of validating computational modeling with nonlinear 3D MHD codes.

The work presented in this paper is focused on understanding the generation of low energy seed runaway electrons and how both collisional damping and magnetic stochasticization can affect them. The RE's are generated in steady tokamak plasmas with low toroidal current and magnetic field produced in the Madison Symmetric Torus (MST) [27]. Density thresholds for both runaway electron onset and suppression are determined with simple variations in gas puffing. The magnetic field stochasticization is varied through application of external RMPs with different poloidal mode number, amplitude, and spatial phase. The RMPs are produced by a poloidal array of saddle coils mounted outside a narrow vertical insulated cut in the otherwise thick conducting shell, a configuration that may approximate the situation in future power-producing fusion reactors where access to the plasma will be extremely limited, and extensive arrays of RMP coils may not be possible. X-ray detectors with different energy ranges and viewing geometries are employed to observe the presence of low-energy runaway electrons, and these detectors are toroidally displaced from the RMP coils in order to sense global effects.

When applied to a pre-existing population of runaway electrons, poloidal mode number  $m = 3$  perturbations are found to suppress the runaways, while perturbations with  $m = 1$  have little effect. This difference is consistent with the difference in magnetic topologies computed by NIMROD [28]. In the absence of an RMP, NIMROD predicts a regular sawtooth cycle, which leads to cyclic distortion of the magnetic topology in the core. The addition of an  $m = 1$  RMP has little effect on the topology, but addition of an  $m = 3$  RMP produces stochasticity in the outer region of the plasma. This, combined with the sawtooth-induced distortion of the central topology, would allow for rapid loss of runaway electrons.

The paper is organized as follows. In section 2, the MST device, RMP system, x-ray detectors, and MST tokamak plasmas are described. In section 3 the observation of runaway electrons in MST and their dependence on the electron density is presented, followed by sections 4 and 5 where the impact of different RMPs on the runaway electron population

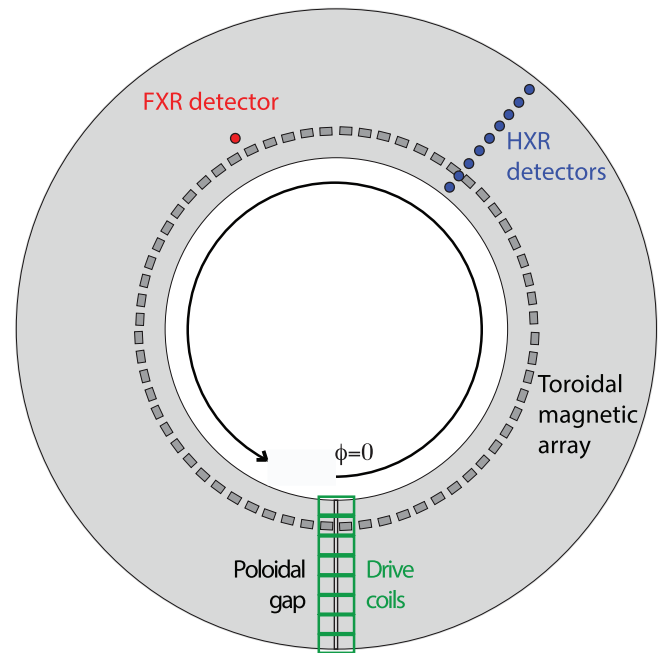


**Figure 1.** Toroidal cross section (top view) of MST. Sketched in green are some of the RMP drive coils (size exaggerated for clarity) around the poloidal gap, in red the position of the FXR detector, and in blue the array of HXR detectors. The location of the toroidal array of magnetic probes is  $61^\circ$  below the inboard midplane.

is described. Section 6 presents the results of the NIMROD simulations, followed by conclusions in section 7.

## 2. Experimental setup

### 2.1. MST and the RMP coils

MST is a toroidal device characterized by major radius  $R_0 = 1.5$  m and minor radius  $a = 0.52$  m. A 5 cm thick aluminum shell surrounds the plasma and serves as both the vacuum vessel and single-turn toroidal field winding. It is largely uniform poloidally and toroidally, except for several portholes with diameters up to 11.43 cm, and two electrically insulated gaps. The poloidal gap, shown in figure 1, extends poloidally at a single toroidal location to allow poloidal flux to enter the vessel. The toroidal gap extends toroidally at the inboard midplane and allows toroidal flux to enter the vessel.

A programmable power supply (PPS) is used to produce the toroidal magnetic field ('BT') [29]. This BT-PPS is comprised of 32 H-bridge modules using high-power insulated-gate bipolar transistors. Each module is powered by a bank of electrolytic capacitors, providing a maximum pulse duration of 120 ms. Two modules form a series-pair providing a maximum output voltage of  $\pm 1800$  V, and 16 of these series-pairs are connected in parallel, yielding a total output current up to  $\pm 25$  kA.

A pulse-forming network (PFN) including a power crowbar diode in the poloidal magnetic field 'BP' circuit provides the plasma current,  $I_p$ . Unlike the PPS, the PFN is a passive circuit that does not provide precise waveform control, which explains the shape of the  $I_p$  waveforms shown, e.g. in figure 2.

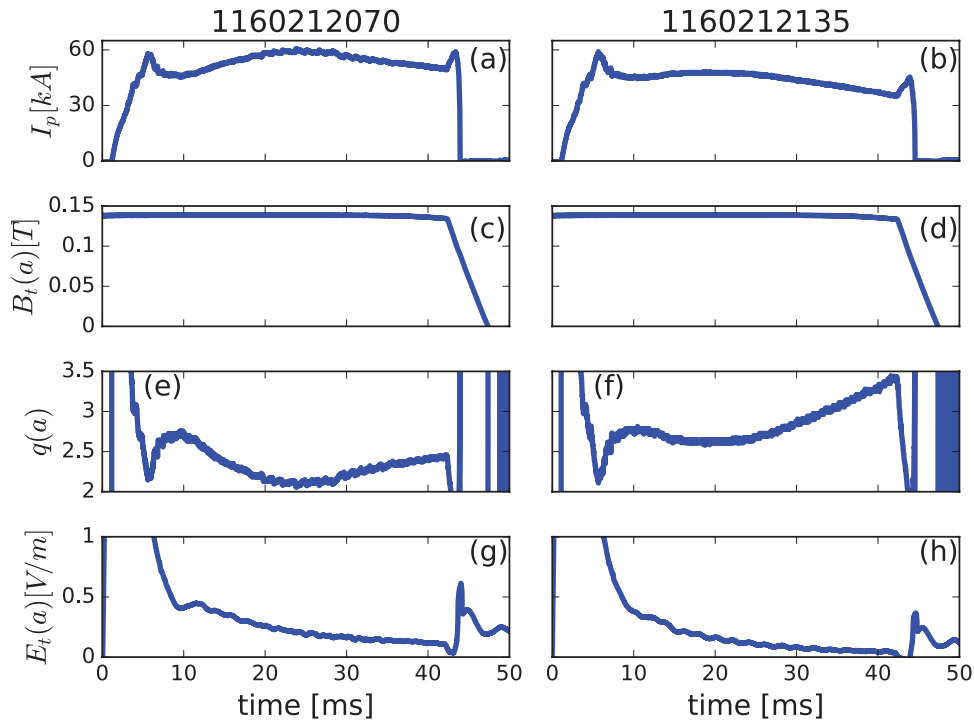


**Figure 2.** From two representative MST tokamak discharges used in this study, temporal waveforms of (a) and (b) toroidal plasma current, (c) and (d) edge toroidal magnetic field, (e) and (f) edge safety factor, (g) and (h) surface toroidal electric field. Shot on the left has a lower edge safety factor than shot on the right.

However, the PFN does provide good shot-to-shot reproducibility for similar plasma current and electron density. More recent tokamak experiments on MST, not discussed in this paper, utilize a new BP-PPS, which does provide very good  $I_p$  waveform control.

The two insulated gaps in the aluminum shell are sources of error fields, but the errors at the poloidal gap are corrected by an active feedback system. The correction system is comprised of 32 evenly spaced radial magnetic field sensing coils coupled to 38 saddle correction coils, the latter sketched in figure 1. The signals from the sensing coils, located inside the vessel [30], are sent to a pair of analog matrix multiplier circuits that decompose the signals into coefficients of a Fourier transform for poloidal mode numbers  $m = 0$  to  $m = 16$ . This controls the current waveforms sent to each of the 38 correction coils.

The correction system is also used to apply RMPs [30], providing an offset to the correction of specific poloidal modes at any desired poloidal phase,  $\theta_{\text{RMP}}$ . The phase angle of the RMP is defined with respect to the location(s) of the maximum inward-pointing radial field. For an  $m = 1$  RMP, for example, a phase of  $\theta_{\text{RMP}} = 0^\circ$  corresponds to the location  $5^\circ$  above the outboard midplane, and a phase of  $\theta_{\text{RMP}} = 90^\circ$  corresponds to the location  $5^\circ$  inboard from the top.

Because the system is toroidally localized around the 6 mm wide poloidal gap, the toroidal mode number  $n$  spectrum of the correction field or RMP is broad, and thus no direct control of individual toroidal modes is possible. Toroidal mode decompositions of the surface magnetic field are performed using measurements from a toroidal array of 64 magnetic

probes located  $61^\circ$  below the inboard toroidal gap, as shown in figure 1.

## 2.2. X-ray detectors

The runaway electrons are observed via the x-rays emitted as bremsstrahlung. Two different systems are used to observe x-rays with energies above 5 keV. One, called fast x-ray (FXR), is a detector with a response time of 20 ns [31]. It is located  $120^\circ$  away toroidally from the correction coils and looks through the plasma from a top-inboard location, through the geometrical axis, to the bottom-outboard side. The energy range where the detector efficiency is maximum is between 4 and 25 keV. The other system is a multi-chord array of hard-x-ray (HXR) detectors [32, 33] with a response time of  $1.2 \mu\text{s}$  and a maximum efficiency from 10 and 150 keV. These are located  $150^\circ$  away toroidally from the correction coils and  $90^\circ$  from the FXR detector, as shown in figure 1, looking through the plasma from the top to the bottom of the machine along different chords. The impact parameters of the chords used in this work are indicated in the figures that include HXR data.

## 2.3. Tokamak discharges

Example waveforms for the two types of tokamak discharge used in this study are shown in figure 2, with a lower- $q(a)$  discharge on the left and a higher- $q(a)$  discharge on the right, where the edge safety factor,  $q(a) \equiv aB_t(a)/[R_0B_p(a)]$ . In these two discharges no external RMP is applied, and the isotope used is deuterium. Figures 2(a) and (b) show the plasma

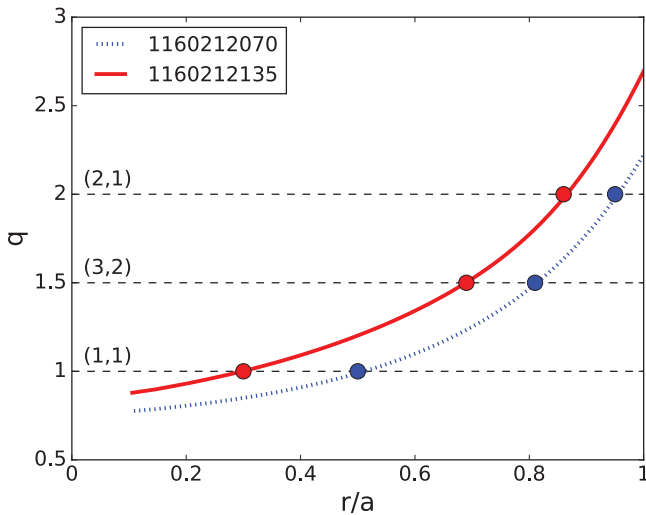


**Figure 3.** Radial profiles of the safety factor for the two discharges in figure 2 at 19 ms, computed with MSTFit. Dashed lines and dots indicate positions of low-order rational surfaces.

current  $I_p$ , and figures 2(c) and (d) show the edge toroidal field  $B_t(a)$ . These discharges have  $I_p \simeq 50$  kA,  $B_t \approx 0.14$  T and a duration of about 45 ms. The discharges end due to the programmed ramp down of  $B_t$ . Figures 2(e) and (f) show the  $q(a)$  values, which are  $q(a) \gtrsim 2.2$  and  $q(a) \gtrsim 2.7$ , respectively, during the period of most experimental interest here, roughly 15–25 ms. Figures 2(g) and (h) show the surface toroidal (mostly parallel) electric field.

Equilibria for these plasmas are reconstructed using MSTFit, a toroidal equilibrium reconstruction code [34]. Radial profiles of the safety factor  $q(r)$  at 19 ms for the two discharges in figure 2 are shown in figure 3. The constraints used for these reconstructions are the edge magnetic diagnostics and the line integrated measurements of the electron density obtained by the far infrared (FIR) interferometer [35]. Also shown in figure 3 are dashed lines and filled circles indicating the positions of low-order rational surfaces. Of course, the rational surfaces are shifted outward comparing the higher- $q(a)$  to the lower- $q(a)$  case. As we will show below, this apparently results in significantly different RE behavior with RMPs in the two cases.

### 3. Generation and suppression of RE's with variations in electron density

In the absence of RE loss mechanisms other than Coulomb collisions, the primary generation (seeding) of RE's occurs when the acceleration of the electrons due to the electric field exceeds the collisional drag acting on them. The threshold condition for the generation of RE's is known as the Dreicer field [1]. Adding to this threshold relativistic considerations such as an upper limit on the electron velocity, and therefore a lower limit on the electric field required to generate any RE, the parallel inductive electric field ( $E_{\text{crit}}$ ) in order to have RE generation is given by [36]

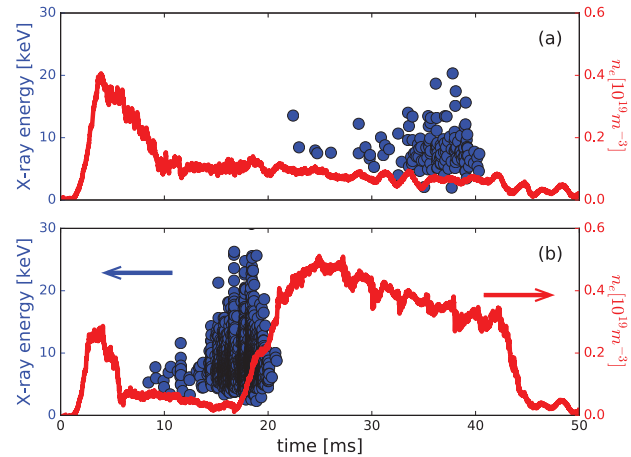


**Figure 4.** X-ray energy (dots) measured by the FXR detector from discharges with (a) a steadily decreasing density and (b) low density followed by increasing density. Each dot represents a single photon. Both plasmas are similar to the lower- $q(a)$  case in figure 2.

$$E_{\text{crit}} = \frac{n_e q_e^3 \ln \Lambda}{4\pi \epsilon_0^2 m c^2}, \quad (1)$$

where the electron density,  $n_e$ , and the Coulomb logarithm,  $\ln \Lambda$ , are the only variables. But the value of  $\ln \Lambda$  varies only slightly for the plasmas of interest, so that  $E_{\text{crit}} \propto n_e$ . Once a runaway electron is present in the plasma, it can accelerate a thermal electron by Coulomb collision up to runaway energies. The two runaways can then do the same to two other thermal electrons, and so on, generating an avalanche of RE's [5]. A more detailed description can be found in [6, 37]. This approach gives an overestimate of the density threshold since it does not include some of the basic features of magnetic confinement devices that may contribute to RE losses. For example, the presence of the magnetic field will lead to synchrotron losses due to Larmor motion, whereas magnetic field fluctuations may cause stochastic particle losses. Also playing a potential role are kinetic instabilities and the interaction with high-Z impurities [9, 37, 38]. Nevertheless, the presence of RE's is expected to be related to  $n_e$ . In particular, RE's are expected at a low enough  $n_e$  for a given parallel electric field.

Motivated by a joint experiment of the International Tokamak Physics Activity—MHD, Disruptions, and Control Topical Group, the dependence of runaway electron onset and suppression on the electron density,  $n_e$ , was evaluated in steady MST tokamak plasmas without applied magnetic perturbations. The density was adjusted in a controlled and reproducible manner with gas puffing. The results are shown in figure 4. The presence of runaway electrons is detected via their emission of x-ray photons. The red traces in each plot are the central line-averaged density measured by the FIR interferometer, and the blue dots correspond to x-rays detected by the FXR detector. In figure 4(a),  $n_e$  slowly decreases with time, and x-rays are observed when  $n_e$  drops below about  $10^{18} \text{ m}^{-3}$ . At about 40 ms, the apparent termination of x-ray

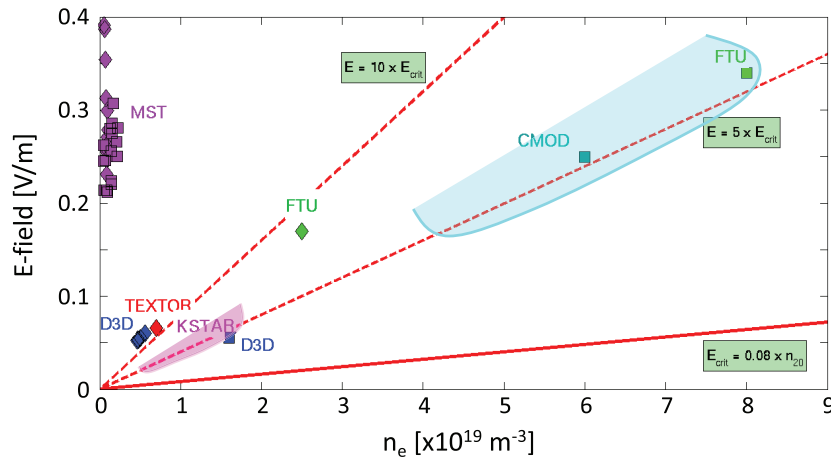


**Figure 5.** Contribution of MST tokamak data to the ITPA—MDC 16 runaway electron database. Onset and suppression data for several devices including MST are indicated by diamonds and squares, respectively. Adapted from [37], with the permission of AIP Publishing.

emission is due to the FXR digitizer reaching the end of its allowable data acquisition time window. In figure 4(b),  $n_e$  at 10 ms is about  $5 \times 10^{17} \text{ m}^{-3}$ , in order to produce RE's early in the shot. Starting around 17 ms,  $n_e$  is steadily increased, and RE's are suppressed when  $n_e$  reaches about  $3 \times 10^{18} \text{ m}^{-3}$ .

Qualitatively, the density dependence of the onset and suppression of runaway electrons is as expected, but the  $n_e$  threshold is lower than that predicted by equation (1), where collisional drag is the only RE loss mechanism considered. This is consistent with the expectation that additional loss mechanisms are in play, and this is consistent with results from other devices, shown in figure 5 [37, 39], which displays one set of key results from the ITPA joint experiment. Here, the onset (diamonds) and suppression (squares) thresholds are shown for several machines as a function of density and toroidal electric field. The solid red line corresponds to the predicted threshold to detect RE's. The MST data, from a number of MST plasmas with different parameters (such as the plasma current, electron density and temperature, and safety factor profile), lie in the top left corner of the plot. The electric field for runaways to emerge in any of the tokamaks in this study is at least five times larger than the predicted  $E_{\text{crit}}$ , and in the case of MST, it is almost two orders of magnitude larger.

Although such a difference seems to indicate the presence of significant loss mechanisms, it can be mainly explained considering that x-rays emitted by RE's can be detected when their density reaches about 0.1% of the bulk electron density. Using the model proposed in [40] where the fraction of the RE population over the bulk electrons is related to a set of basic tokamak plasma parameters, it is found that, in MST, RE's are measurable when  $V_{\text{loop}} = 2.35 \text{ V}$  (or  $E \simeq 0.25 \text{ V m}^{-1}$ ),  $T_e = 90 \text{ eV}$ , and  $n_e \sim 10^{18} \text{ m}^{-3}$  [41]. These values of electric field and density are quite similar to those shown in figure 5. In the model,  $V_{\text{loop}}$  and  $T_e$  are estimated from power balance (assuming only Ohmic heating) and Ohm's law starting from the toroidal plasma current, the toroidal magnetic field, and the major and minor plasma radii.  $V_{\text{loop}}$  and  $T_e$  are then used to estimate  $E_{\text{crit}}$ .

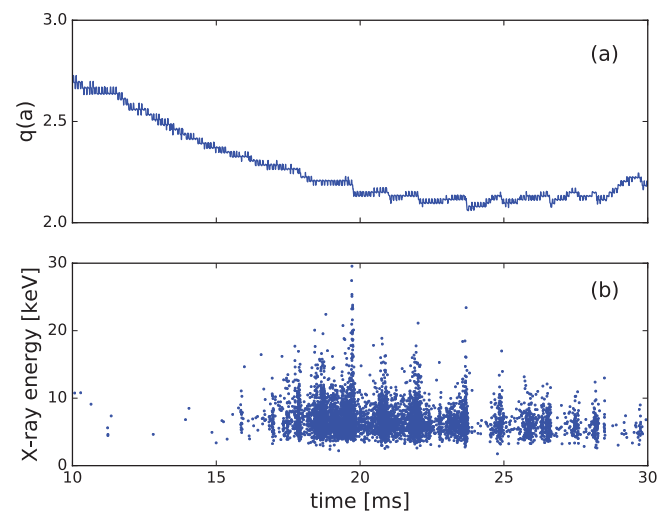


**Figure 6.** (a) Safety factor at the edge and (b) x-ray photon energies measured by the FXR detector for discharge 1160212070. Each dot represents a single photon.

## 4. Impact on RE's of an $m = 3$ RMP

### 4.1. RMP effects in low- $q(a)$ equilibrium

We now present the impact on RE's of the application of an  $m = 3$  RMP with two different spatial orientations, or phases. All of the data presented here and in the remainder of the paper are in low-density plasmas in which runaway electrons are generated. The electron density,  $n_e$ , after plasma startup is maintained around  $5 \times 10^{17} \text{ m}^{-3}$ , and always below about  $7 \times 10^{17} \text{ m}^{-3}$ . Thus, as discussed in section 3, RE's are generated during the early part of the discharge.

In figure 6(b) is shown a typical time evolution of the x-rays observed by the FXR detector, where each dot corresponds to a detected x-rays whose energy is indicated by the vertical axis. Plot 6(a) is a zoom of plot 2(e) from 10 ms to 30 ms. Several observations can be made. Few x-rays are observed at the beginning of the time window, as the plasma current is ramping up and the edge safety factor is ramping down, whereas a large number are present after 15 ms with

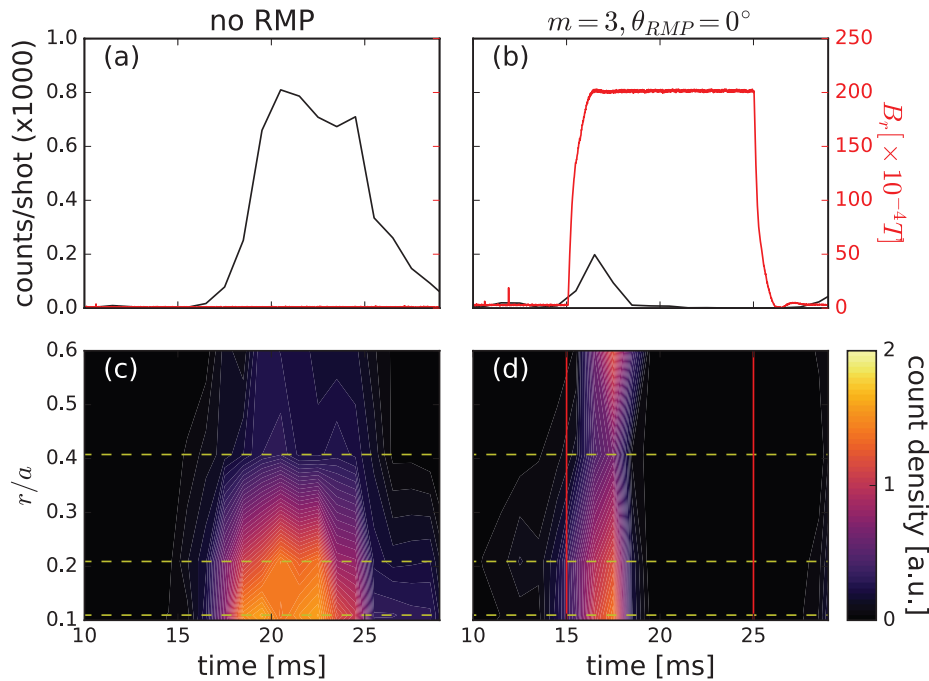


**Figure 7.** Based on an average of similar shots, comparison of two otherwise similar low-density discharges without and with an RMP. An  $m = 3$  RMP is applied to the discharges on the right, with a spatial poloidal phase,  $\theta_{RMP} = 0^\circ$ . All plasmas are similar to the lower- $q(a)$  case in figure 2. Red waveform in (b) corresponds to RMP, measured at the poloidal gap. Black waveforms in (a) and (b) reflect x-ray emission for energies  $E > 5$  keV measured by the FXR detector, binned every 1 ms, and averaged over several similar discharges. Data from three HXR detectors shown in (c) and (d), with colors indicating the number of x-rays with  $E > 10$  keV in 1 ms time intervals, normalized by plasma volume observed by each detector. Impact parameter of each detector indicated by horizontal dashed line. Vertical red lines in (d) correspond to start and end of RMP waveform.

a subsequent gradual decrease in the x-ray count over time. One also observes a bursty behavior of the emission with peaks about every 1 ms. The bursts are associated with MHD activity observed in the  $q(a)$  time evolution, which we believe to be sawtooth crashes. They can be explained by a periodic flattening of core RE profiles during the sawtooth, if not a complete flushing of seed RE's from the core, when the highest-energy electrons collide with the wall and give up all of their energy thus showing a temporary maximum in the x-ray energy.

A comparison of discharges with an  $m = 3$  RMP and a reference case, with no RMP, is shown in figure 7. The discharges shown are similar to the lower- $q(a)$  shot on the left in figure 2. Data from the reference case are shown in figures 7(a) and (c). Figure 7(a) contains data from the FXR detector, showing the average number of x-rays over several discharges with energies  $E > 5$  keV. The x-ray average is calculated every 1 ms. The contour plot in figure 7(c) contains data from the HXR detector radial array, showing the number of x-rays with  $E > 10$  keV over each 1 ms time interval, normalized by the volume observed by each of the detectors. Dashed lines indicate the impact parameter of each detector, not including the detectors at  $r/a = 0$  and  $r/a = 0.6$ .

Two main observations can be made from figures 7(a) and (c). The first is that while the emission of lower-energy x-rays extends from about 15–30 ms, the emission of higher-energy x-rays is limited to an interval of only 17–25 ms. The second is that the emission is observed mainly by the detectors that

sample the center of the plasma, suggesting that the x-rays observed are emitted due to electron–ion bremsstrahlung rather than through target emission (i.e. electrons hitting the wall). Both these results will be discussed in more detail later in this section.

The radial profile of the safety factor  $q$  shown in figure 3 shows that modes with  $m = 1$ ,  $m = 2$ , and  $m = 3$  are internally resonant. Hence, an externally applied RMP with any of these periodicities could have an effect on the magnetic topology and the confinement of runaway electrons. Figures 7(b) and (d) show data from the FXR and HXR detectors, respectively, when an  $m = 3$  RMP is applied from 15–25 ms with a spatial phase,  $\theta_{RMP} = 0^\circ$ . The amplitude of the radial magnetic field measured by the sensing coils lying between the RMP drive coils and the plasma is  $B_r(a) \simeq 20$  mT, corresponding to  $B_r(a)/B(a) \simeq 14\%$ . Due to the geometry of drive coils, each toroidal harmonic  $n$  at the edge has a toroidally-averaged amplitude of  $\delta B \simeq 0.4$  mT ( $\delta B/B(a) \simeq 0.28\%$ ). When the RMP is turned on, a short burst of x-rays, lasting a few ms, is measured by both x-ray detector systems. After that, no x-rays are measured by either system. An important feature of the short burst is that it is spread over more HXR chords than the emission without RMP, suggesting a flattening of the runaway electron profile, possibly spreading RE's into regions of the plasma where primary generation was not possible.

To better understand these results, a scan of the  $m = 3$  RMP amplitude has been performed, as shown in figure 8. Figure 8(a) shows the number of x-rays with energies

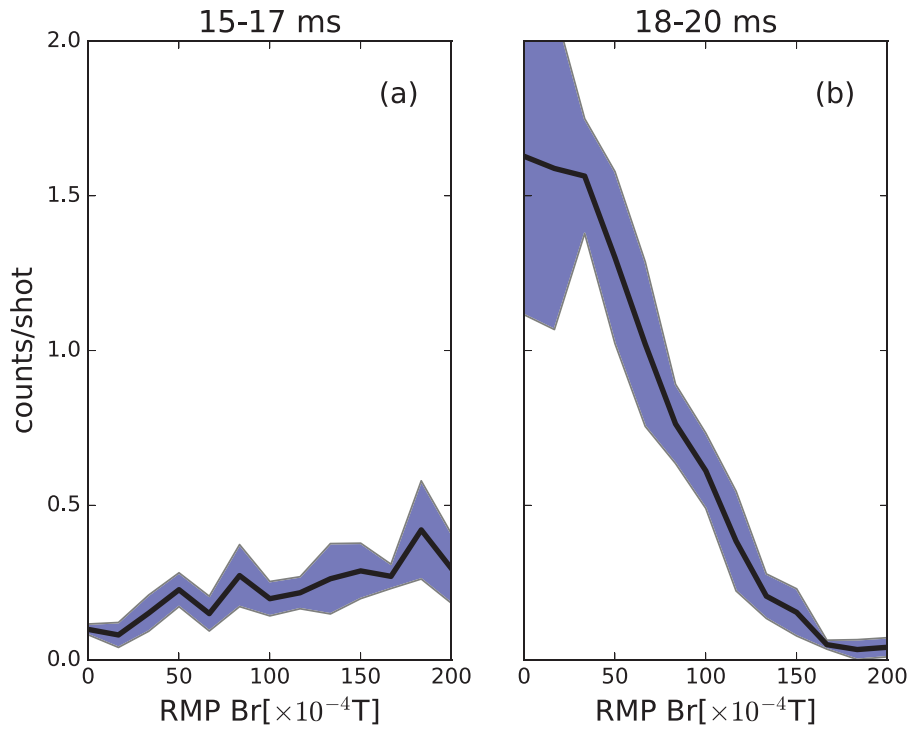


**Figure 8.** With a shot-by-shot scan of  $m = 3$  RMP amplitude, x-ray emission above 5 keV measured by the FXR detector as function of RMP amplitude from (a) 0–2 ms after RMP start and (b) 3–5 ms after RMP start. RMP starts at 15 ms, with  $\theta_{RMP} = 0^\circ$ .

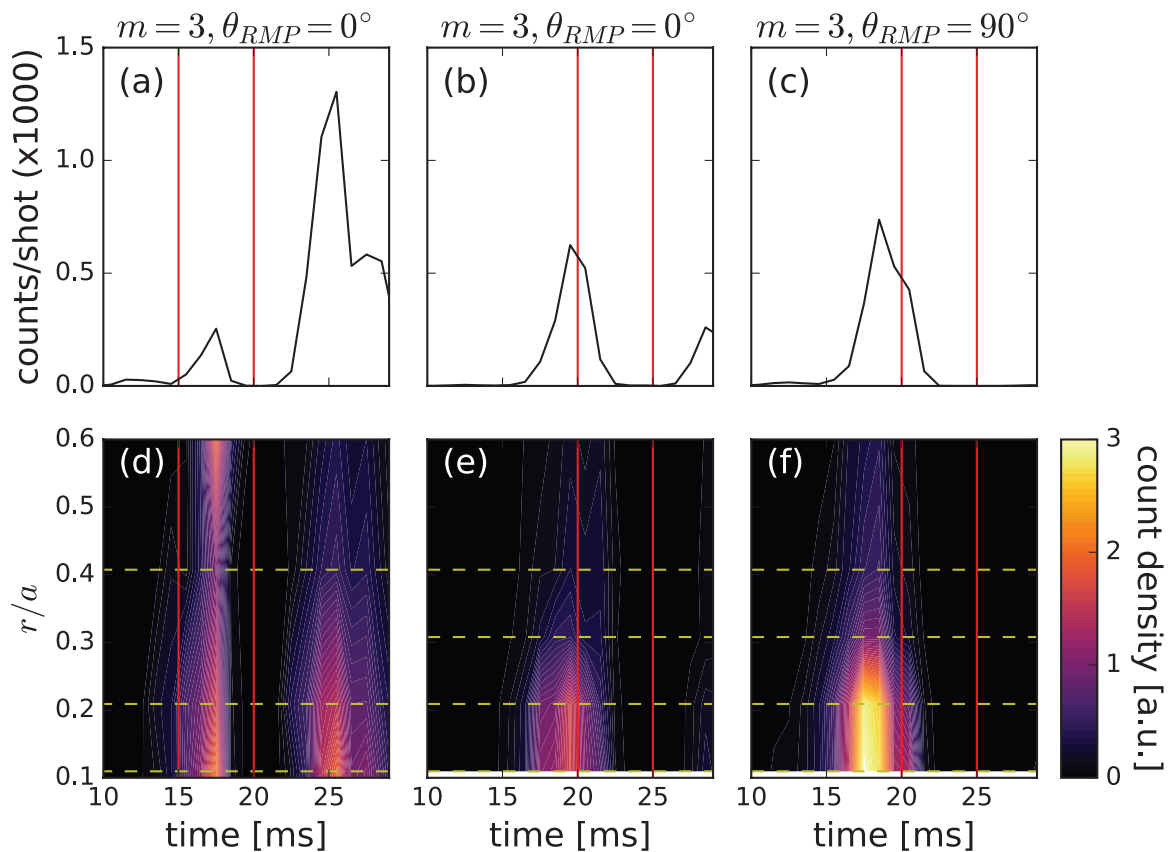


**Figure 9.** X-ray data for different  $m = 3$  RMP timings and spatial phases. Data from FXR detector shown in (a)–(c), and data from HXR detectors shown in (d)–(f), all displayed in the manner described in figure 7. Vertical red lines correspond to start and end of RMP waveforms.

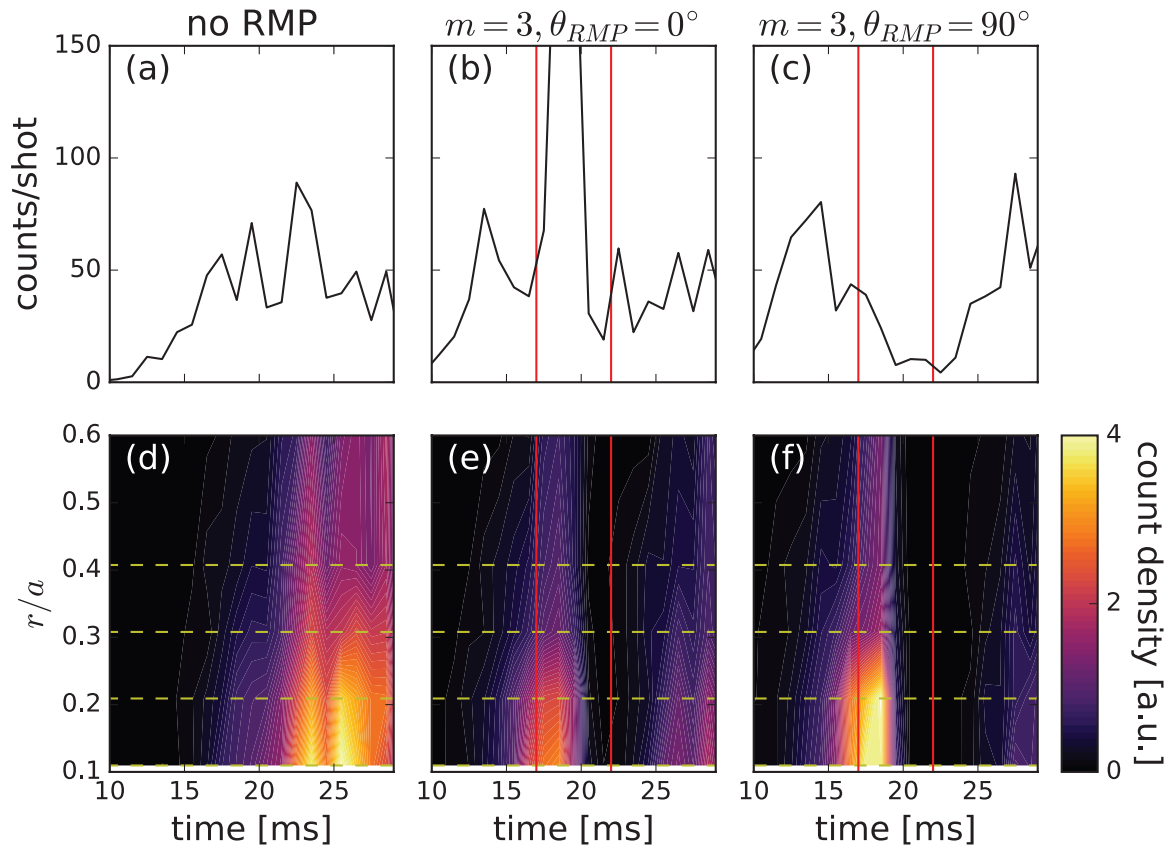


**Figure 10.** X-ray data for different  $m = 3$  RMP spatial phases in higher- $q(a)$  plasmas similar to that shown in figure 2. Data from FXR detector shown in (a)–(c), and data from HXR detectors shown in (d)–(f), all displayed in the manner described in figure 7. Vertical red lines correspond to start and end of RMP waveforms.

$E > 5$  keV measured by the detector in the first 2 ms of RMP application, as a function of the radial magnetic field applied. It confirms that an increase in the  $m = 3$  RMP early in time increases the x-ray count. Figure 8(b) shows the number of x-rays with  $E > 5$  keV measured from 3–5 ms after the start of the RMP. Above about 3.5 mT, x-ray emission drops as the RMP amplitude increases, and above about 16 mT, the maximum suppression is achieved.

RMPs with  $m = 3$  of shorter duration and with the poloidal phase rotated by  $90^\circ$  have also been applied. The results are shown in figure 9, where the RMP application time windows are indicated by red vertical lines. In figures 9(a), (b), (d) and (e) the RMP has a poloidal phase of  $\theta_{RMP} = 0^\circ$ , while figures 9(c) and (f) correspond to a phase of  $\theta_{RMP} = 90^\circ$ . The timing of RE suppression moves with the application time of the RMP. The radially extended x-ray emission during the first few ms of RMP application is clear for the earlier application in figures 9(a) and (d), while it is not clearly observed in the later application in figures 9(b), (c), (e) and (f). This is seen in figures 9(e) and (f), where the emission is confined to the central HXR chords. It is important to observe that for the late RMP application cases, figures 9(b), (c), (e) and (f), the x-ray emission is already decreasing before the RMP application.

Once the perturbation is turned on a higher decreasing slope is observed.

#### 4.2. RMP effects in higher- $q(a)$ equilibrium

With the goal of moving the  $m/n = 3/2$  rational surface further inside the plasma, discharges with  $q(a) \gtrsim 2.7$  have been produced. An example of these discharges is the shot on the right in figure 2, whose (red) safety factor radial profile is shown in figure 3. Plots (a) and (d) of figure 10 show the FXR and HXR data in the absence of an RMP. Two main differences are evident between these and plots (a) and (c) of figure 7 (which referred to the lower- $q(a)$ , no RMP case). One is the lower amount of x-rays detected, which may reflect the lower  $E_{tor}$  required for the lower plasma current in the higher  $q(a)$  case (see figure 2). The other is the continuous emission, as opposed to a consistent decrease of x-rays observed in figure 7(a) after 25 ms. This may be related to the lower level of MHD activity observed in these discharges.

The  $m = 3$  RMPs are applied to these higher- $q(a)$  plasmas from 17 to 22 ms, with results shown in figures 10(b), (c), (e) and (f). The case with a phase  $\theta_{RMP} = 90^\circ$  is shown in figures 10(c) and (f), while the case with  $\theta_{RMP} = 0^\circ$  phase is

shown in figures 10(b) and (e). The results apparently depend on both the phase and the x-ray detector considered. In figures 10(c), (e) and (f), suppression of the x-ray emission is observed during application of the RMP, while figure 10(b) shows an increase of x-ray emission.

#### 4.3. Discussion

We have shown that the impact of an  $m = 3$  RMP on RE's depends on the target equilibrium as well as the timing and spatial phase of the RMP. One clear result is that in the  $q(a) \gtrsim 2.2$  plasmas, the x-ray emission, reflecting the RE population, decreases as the RMP amplitude increases, for an RMP amplitude of 3.5 mT or more. And, almost complete suppression is observed with an amplitude greater than 16 mT. A possible mechanism underlying this suppression, based on the imposition of magnetic stochasticity, is found from computational modeling and will be described in section 6.

Several other observations in the discharges with  $q(a) \gtrsim 2.2$  are not yet fully understood. Even in the absence of an RMP, figure 7(a), x-ray emission decreases after 25 ms even though the electron density is still below the threshold established in section 3. A possible explanation, that will require further investigation, is the presence of MHD activity which may reduce the high-energy electron population at the same time that the toroidal electric field decreases (see figure 6), thereby reducing the number of electrons that can be accelerated.

Another puzzling result is the peak of RE's observed in the first 2 ms of the  $m = 3$  RMP application. This is observed mainly for early application of the RMP, with a possible dependence on the phase of the RMP and on the equilibrium. This x-ray peak seems to be related to a loss of RE confinement, given that x-rays are also observed by the HXR detectors not viewing the core. This observation seems to apply more clearly to the lower- $q(a)$  case, and less so to the higher- $q(a)$  case. The strong peak observed at the application of the RMP in figure 10(b) is not observed by the edge HXR detectors in figure 10(e). Moreover, the x-ray count in figure 10(b) is larger than those observed at any other time in this equilibrium and is comparable to the lower- $q(a)$  case.

Further analysis is needed to understand these observations, but a partial explanation for some of this behavior, particularly that shown in figure 10(b), may be tied to healing rather than breaking of flux surfaces by the RMP. In the J-TEXT tokamak, application of a sufficiently strong  $m/n = 2/1$  RMP around a disruption enhanced rather than suppressed runaway electron generation [42]. The thermal quench associated with the disruption is commonly associated with stochasticization of the magnetic topology. The explanation posited for the J-TEXT observation was that the RMP produced magnetic islands, which correspond to regions of intact flux surfaces. For this mechanism to apply to MST would necessitate a region of at least weak stochasticity, before application of the RMP, in the steady plasmas.

Complicating all of this analysis is the fact that fine control of the RE's is not possible, so there is a non-negligible

shot-to-shot variability in the x-ray emission before and after application of the  $m = 3$  RMP. The variability of the x-ray emission in the later part of the discharge seems to be related to the presence of the RMP. Figure 9, for example, shows that the RMP seems to stimulate RE's once it is turned off, but only for  $\theta_{\text{RMP}} = 0^\circ$ , and x-ray emission is not always observed by all of the detectors.

The unexpected dependence on RMP phase could be explained by the coupling of the RMP with static error fields. Such coupling can modify the toroidal and poloidal spectrum of the perturbation applied, and this can have an impact on RE mitigation as was observed on ASDEX-Upgrade [15]. A similar unexpected dependence on RMP phase was also observed in rotation braking experiments in MST reversed-field pinch plasmas [43]. Applying an  $m = 1$  RMP with different phases to rotating plasmas, a dependence on the phase of the RMP-induced deceleration time of  $m = 1$  modes was observed. The reason(s) for this dependence have not yet been determined, but it corroborates the possibility of a coupling between the RMP and certain static error fields.

Some of the puzzling observations in this paper could suggest the possibility that the observed x-rays are emitted by high-energy electrons striking the wall, i.e. target emission, rather than by collisions with plasma ions. However, there are two reasons to doubt this hypothesis. First, these plasmas were also observed along a toroidally-viewing chord, effected by moving the FXR detector to a tangential port, which increased the sample volume and imaged much more of the wall compared to the radially-viewing chords discussed above [44, 45]. But the tangential view showed results similar to those observed looking radially. A second piece of evidence came from the observation of plasma-wall interaction through a camera viewing  $D_\alpha$  emission from the poloidal gap, as described in [30]. No clear changes in  $D_\alpha$  emission from the wall were observed, either when the RMP was applied or when it was turned off. Therefore, these observations tend to confirm that what is observed are mainly x-rays emitted by bremsstrahlung rather than target emission. Another possible explanation would be the presence of a particular target for the RE's that is not observed by the spatially localized detectors.

## 5. Impact on RE's of $m = 1$ and $m = 2$ RMPs

The effect of  $m = 1$  and  $m = 2$  RMPs on lower- $q(a)$  plasmas has also been studied to a limited extent. The results are mixed and not yet well understood, but we include them for completeness. The  $q(a) \sim 2.2$  equilibrium has been chosen because of the proximity of the  $m/n = 1/1$  and  $m/n = 2/1$  resonant surfaces to the boundary and the drive coils, where the RMP is stronger, and because of the relatively large number of x-rays generated in the absence of an RMP.

In figure 11, the effects on x-ray emission of an  $m = 1$  RMP applied from 15 to 20 ms are shown. A case with RMP phase  $\theta_{\text{RMP}} = 0^\circ$  is shown in figures 11(a) and (c), and a case with  $\theta_{\text{RMP}} = 90^\circ$  is shown in figures 11(b) and (d).

For an RMP amplitude similar to that applied in the  $m = 3$  RMP cases, the impact of the  $m = 1$  RMP is once again phase

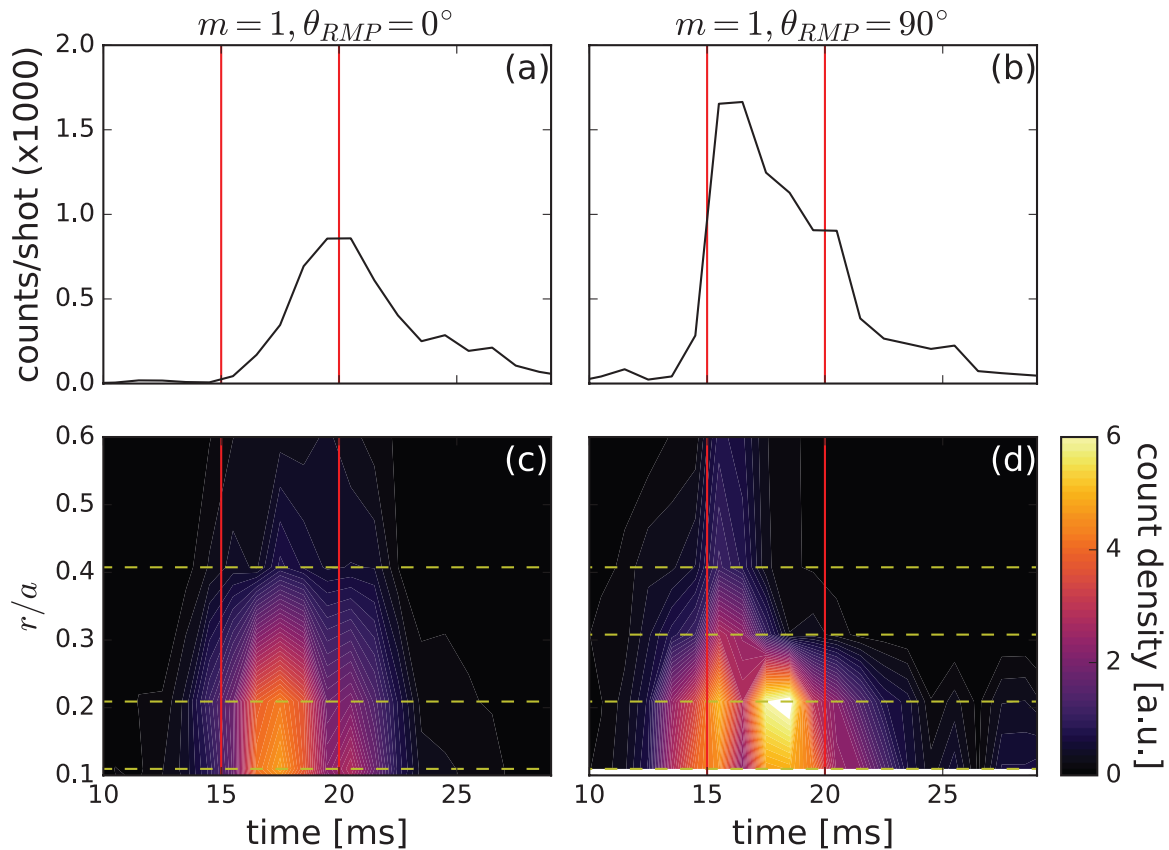


**Figure 11.** X-ray data for different  $m = 1$  RMP spatial phases in low- $q(a)$  plasmas. Data from FXR detector shown in (a) and (b), and data from HXR detectors shown in (c) and (d), all displayed in manner described in figure 7. Vertical red lines correspond to start and end of RMP waveforms.

dependent, but full suppression is not observed in either case. For phase  $\theta_{RMP} = 0^\circ$ , the x-ray emission waveform and amplitude measured by the FXR detector are similar to that of the no-RMP reference case shown in figure 7(a). For phase  $\theta_{RMP} = 90^\circ$ , the FXR-measured emission peaks at an amplitude about twice that of the reference case and subsequently decreases. Perhaps coincidentally, the FXR x-ray count at 20 ms, the end of the RMP period, is comparable in both cases. The higher-energy x-ray emission measured by the HXR detectors portrays a somewhat different story, particularly in the  $\theta_{RMP} = 90^\circ$  case, which exhibits two distinct peaks.

Application of an  $m = 2$  RMP led to the most ambiguous results. In contrast to the  $m = 3$  and  $m = 1$  cases, a similar-amplitude  $m = 2$  RMP often caused partial, sporadic drops in the toroidal plasma current, apparently linked to MHD activity. The RMP amplitude at which the plasma current began to be affected depended on the RMP phase. And to further complicate matters, the effect on the plasma current waveform was not shot-to-shot reproducible, for the same programmed conditions. This in turn led to considerably greater variation shot to shot in the x-ray emission. So while the  $m = 2$  RMP clearly had an impact on the discharge, the direct impact on the runaway electrons was difficult to discern.

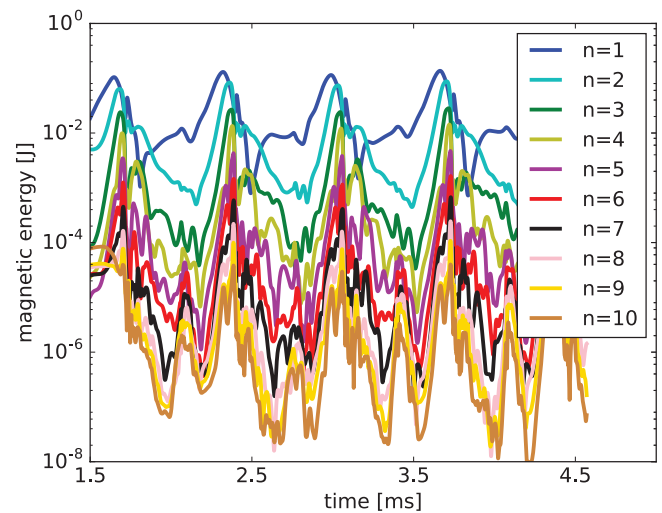


**Figure 12.** Computed evolution of magnetic fluctuation spectrum, in terms of toroidal mode number, without RMP.

## 6. Computational modeling

To understand the topological effects of the  $m = 1$  and  $m = 3$  RMPs on the magnetic field, nonlinear resistive magneto-hydrodynamic (MHD) simulations of the  $q(a) = 2.2$

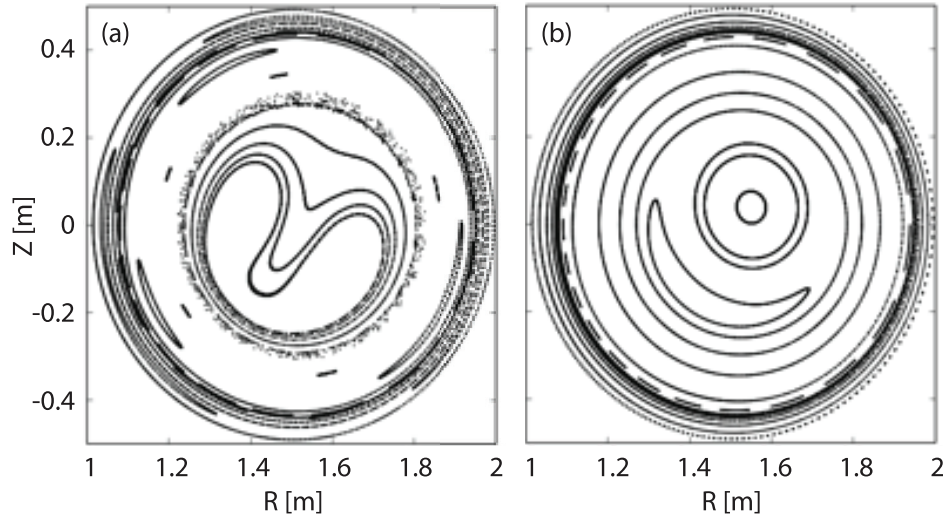


**Figure 13.** Poincaré surfaces of section showing magnetic topology from the simulation without RMP (a) at  $t = 1.73$  ms, the high-energy phase of the sawtooth, and (b) at  $t = 2.20$  ms, the low-energy phase.

equilibrium have been performed. MST tokamak discharges have  $\beta < 1\%$ , so we use a simple model without pressure ( $p$ ) or mass density ( $\rho$ ) evolution, treating  $\rho$  as a fixed, uniform parameter:

$$\rho \left( \frac{\partial}{\partial t} \mathbf{V} + \mathbf{V} \cdot \nabla \mathbf{B} \right) = \frac{1}{\mu_0} (\nabla \times \mathbf{B}) \times \mathbf{B} + \nabla \cdot \rho \nu \left[ \nabla \mathbf{V} + \nabla \mathbf{V}^T - \frac{2}{3} (\nabla \cdot \mathbf{V}) \mathbf{I} \right] \quad (2)$$

$$\frac{\partial}{\partial t} \mathbf{B} = \nabla \times \left( \mathbf{V} \times \mathbf{B} - \frac{\eta}{\mu_0} \nabla \times \mathbf{B} \right), \quad (3)$$

where  $\eta$  is the electrical resistivity,  $\nu$  is viscous diffusivity, and  $\mathbf{I}$  is the identity tensor. The simulations are performed with the NIMROD code [28] in the geometry of a circular-cross-section torus of aspect ratio  $R_0/a = 3$ , which is representative of MST. The equilibrium  $R\mathbf{B}_\phi$ -profile from MSTFit [34] is read into the NIMEQ Grad–Shafranov solver [46], and the equilibrium is recomputed with NIMROD's spatial representation, taking  $p = 0$ . Our NIMROD computations treat this equilibrium as a steady state and solve for nonlinear perturbations from this state, including any axisymmetric component that may develop.

Computations that model plasmas with RMPs include a representative surface perturbation,

$$\mathbf{B} \cdot \hat{\mathbf{n}}|_{r=a} = \frac{B_{\text{rmp}}}{\pi R} \cos(m\theta) \left[ \frac{l_{\text{gap}}}{2} + R_0 \sum_{n=1}^{N/2} \sin\left(n \frac{l_{\text{gap}}}{2R_0}\right) \cos(n\phi) \right], \quad (4)$$

where  $m$  is the poloidal wavenumber of the imposed perturbation,  $B_{\text{rmp}}$  is its magnitude,  $R_0$  is the major radius, and  $l_{\text{gap}}$  is the spatial scale of the poloidal gap. The computations use NIMROD's Fourier expansion to represent toroidal variations, where  $N$  represents the largest harmonic. The expansion shown in equation (4) truncates the perturbation to avoid driving the shortest toroidal wavelengths in a computation. The applied

$B_{\text{rmp}}$  matches the nominal experimental value of 20 mT, and  $l_{\text{gap}}$  is chosen to produce a projection of approximately 1/100 onto the low- $n$  Fourier components [47]. Computations with RMPs are initialized with vacuum-field distributions of the RMP fields, whereas those without RMPs include small random perturbations to initiate any linearly unstable modes. Plasma responses to RMPs develop during early transients. The computations reported here have Lundquist number  $S = 9.4 \times 10^4$  with magnetic Prandtl number ( $\mu_0 \nu / \eta$ ) of unity. The value of  $S$  in the core of MST tokamak discharges is somewhat larger, but unlike the experiment, wherein  $S$  decreases from the core to the edge, the computations have  $\eta$ - and  $\nu$ -profiles that are essentially uniform, except for a thin dissipative layer near the boundary. Numerically, we have used a  $32 \times 32$  (radial  $\times$  azimuthal) mesh of bicubic elements with toroidal Fourier components  $0 \leq n \leq 10$ .

From figure 3 we note that the  $q = 1$  surface is at  $r \simeq a/2$ , and linearized computations show that (1,1) internal-kink and (2,2) modes are unstable in this profile. All other resonant modes are linearly stable. In the absence of an RMP, the nonlinear evolution of the magnetic fluctuation spectrum, shown in figure 12, displays a sawtooth cycle with a period of approximately 0.7 ms, and it is plausible that the oscillations of slightly longer period that are evident in the experimental data, starting around 20 ms in figures 2(a) and (e), are from sawtoothing. The evolution of the magnetic topology during a computed sawtooth cycle is shown by the magnetic Poincaré surfaces of section in figure 13. Although the sawtooth perturbation is large, toroidal magnetic flux surfaces between the central sawtooth structure and the wall remain intact.

When an RMP is applied, with an amplitude comparable to that in the experiment, the energy in the  $n > 0$  components of  $\mathbf{B}$  is larger than those from the kink dynamics, but sawtoothing still occurs. Figure 14 shows a comparison of magnetic topologies over a sawtooth cycle from simulations with separately applied  $m = 1$  and  $m = 3$  perturbations. In the computation with the  $m = 1$  perturbation, there are intact flux

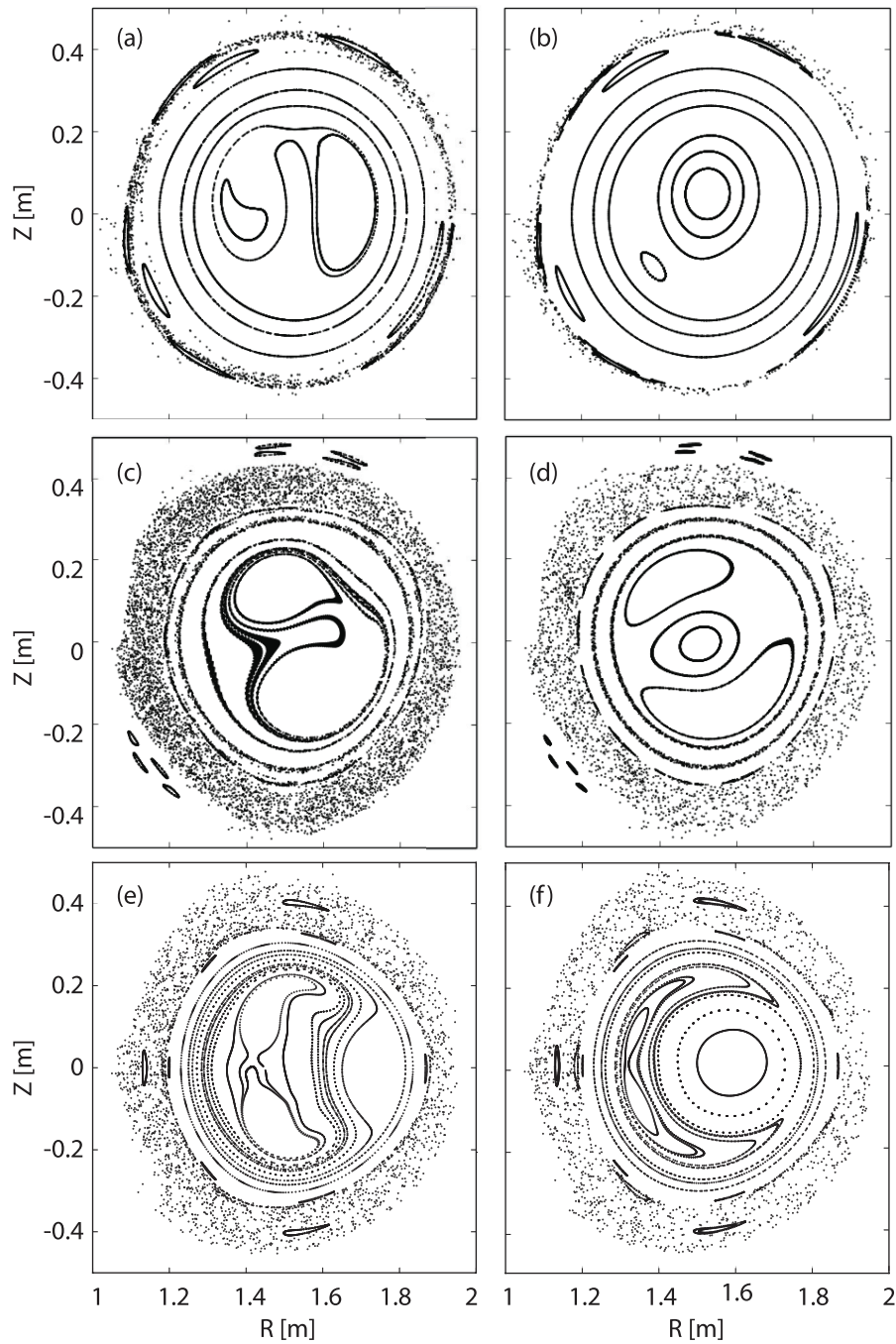


**Figure 14.** Poincaré surfaces of section showing magnetic topology from the simulations with  $m = 1$  RMP at (a) the high-energy phase and (b) the low-energy phase and with  $m = 3$  RMP at (c) the high-energy phase and (d) the low-energy phase. Plots (e) and (f) contain the high-energy and low-energy phases, respectively, with  $m = 3$  RMP shifted by  $90^\circ$  relative to what is shown in plots (c) and (d).

surfaces surrounding the sawtooth structure throughout the cycle. In contrast, the computation with the  $m = 3$  perturbation always has chaotic scattering over the outer 2/5 of the minor radius.

The poloidal phase of the RMP is the same for the cases in figures 14(a)–(d), with the maximum inward pointing radial field located at the inboard midplane for an  $m = 1$  RMP, while it is shifted by  $90^\circ$ , pointing inward from the top, for the data in figures 14(e) and (f). The computations show that a change in the absolute phase of the perturbation does not substantially modify the extent of the outer stochastic region. The changes

in the core topology are possibly due to slight differences in the times in the sawtooth cycle at which the Poincaré plots are produced. This result is consistent with the presence of a static error field in the experiment, not included in the simulations, as suggested in section 4.3, that couple with the applied RMP modifying its spectrum when the phase changes, and therefore the impact on the RE's [15].

To determine which components of the  $m = 3$  magnetic perturbation are responsible for the scattering, we consider the topology resulting from vacuum-field perturbations with scaled amplitudes, superposed on the equilibrium. Figure 15(a) shows

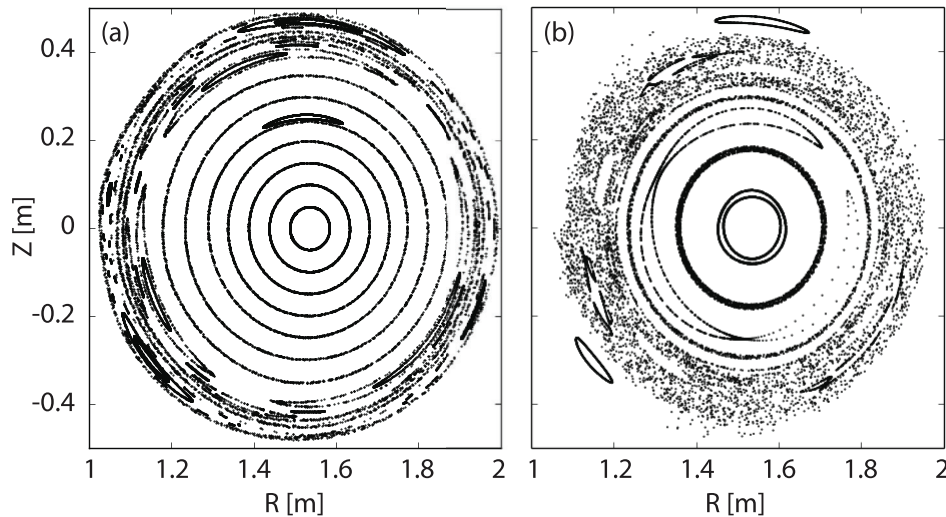


**Figure 15.** Poincaré surfaces of section for vacuum-field  $m = 3$  perturbation of amplitudes (a) 5 mT and (b) 20 mT superposed on the MST  $q(a) = 2.2$  equilibrium.

the resulting magnetic topology with the amplitude reduced by 75%, which may be compared with the full-amplitude topology in figure 15(b). The reduced-amplitude topology clearly shows distinct island chains with mode numbers  $m/n = 3/3, 3/2, 8/5, 5/3,$  and  $4/2$  that at the full perturbation amplitude overlap and yield chaotic scattering. All of these components are internally resonant (blue curve in figure 3).

We note that while the perturbation is geometrically  $m = 3$  at the surface, the toroidal geometry inherently couples other  $m$ -values, and the  $n$ -spectrum that approximates the experiment's narrow gap is broad. We surmise that the substantial layer of chaotic scattering near the wall of the simulation with an  $m = 3$  perturbation would enhance transport for the charged particle populations that largely follow  $\mathbf{B}$ . This may be the case for the RE population that is suppressed by  $m = 3$  RMP in MST, as discussed in section 4. That edge flux surfaces remain intact without an RMP and with an  $m = 1$  RMP, where experimental RE's are less affected, is consistent with this hypothesis. However, the spatially resolved measurements of figures 7, 9–11 show the largest x-ray signals coming from the core of MST discharges, where the  $q = 1$  resonant structure dominates the magnetic topology, regardless of RMP amplitude, wavenumber or even presence. Thus, this magnetic structure must also have a role in transporting the RE's to an edge chaotic region. How that might be occurring can be addressed by tracing RE orbits in the different simulated magnetic topologies, as done in [48]. This aspect and the effects of  $m = 2$  perturbations are left for future study.

## 7. Conclusions

This paper has presented initial studies of RE generation in low-density, low-current, low-magnetic-field tokamak plasmas in MST and their suppression by externally applied RMPs. Three important results are shown. The first is that RE's can be experimentally generated at very low densities and suppressed by a density increase with results comparable

to other machines. The second is that in experiments,  $m = 3$  RMPs tend to strongly suppress RE's activity, while  $m = 1$  RMPs do not have nearly the same clear, suppressing effect. The third is that nonlinear resistive MHD simulations of these experiments show chaotic scattering of edge magnetic fields with an  $m = 3$  RMP but not with an  $m = 1$  RMP. The qualitatively distinct effect of the simulated  $m = 3$  RMP provides a plausible explanation for the reduction of RE's observed with the  $m = 3$  RMP. However the invoked influence of sawteeth on the RE orbits and whether this is the nature of the bursty MHD activity observed in the lower  $q(a)$  discharges remains to be proven.

As discussed above, there are still several open questions regarding these topics in both the experiment and computation. In the experiment, these include puzzling details of RMP effects for different combinations of  $m$  values and spatial RMP phases. In the computation, they focus on the possible role of the core  $q = 1$  resonant structure in coupling RE transport to a chaotic edge region. We plan for both of these topics to be addressed in future studies of tokamaks in MST.

## Acknowledgments

We thank the MST team for help with gathering data, and we thank C. Paz-Soldan for help in modeling MST runaway electron data. This material is based upon work supported by the U.S. Department of Energy Office of Science, Office of Fusion Energy Sciences program under Awards No. DE-FC02-05ER54814, DE-FC02-08ER54975, DE-SC0018001, DE-SC0020245 and the U.S. Department of Energy Computational Sciences Graduate Fellowship program. The computational part of this research was performed using the computer resources and assistance of the UW-Madison Center For High Throughput Computing (CHTC) in the Department of Computer Sciences. The CHTC is supported by UW-Madison, the Advanced Computing Initiative, the Wisconsin Alumni Research Foundation, the

Wisconsin Institutes for Discovery, and the National Science Foundation, and is an active member of the Open Science Grid, which is supported by the National Science Foundation and the U.S. Department of Energy's Office of Science.

The numerical data presented in this paper are available in the supplementary material (available online at [stacks.iop.org/NF/60/046024/mmedia](https://stacks.iop.org/NF/60/046024/mmedia)).

## ORCID iDs

S. Munaretto  <https://orcid.org/0000-0003-1465-0971>

## References

- [1] Dreicer H. 1959 *Phys. Rev.* **115** 238
- [2] Dreicer H. 1960 *Phys. Rev.* **117** 329
- [3] Wilson C.T.R. 1925 *Proc. R. Soc.* **37** 32D
- [4] Sokolov Y.A. 1979 *JETP Lett.* **29** 244
- [5] Rosenbluth M.N. and Putvinski S.V. 1997 *Nucl. Fusion* **37** 1355–62
- [6] Helander P., Eriksson L.-G. and Andersson F. 2002 *Plasma Phys. Control. Fusion* **44** B247
- [7] Hender T.C. et al 2007 *Nucl. Fusion* **47** S128–202
- [8] Nygren R., Lutz T., Walsh D., Martin G., Chatelier M., Loarer T. and Guilhem D. 1997 *J. Nucl. Mater.* **241** 522
- [9] Paz-Soldan C. et al 2019 *Nucl. Fusion* **59** 066025
- [10] Commaux N. et al 2011 *Nucl. Fusion* **51** 103001
- [11] Hollmann E.M. et al 2013 *Nucl. Fusion* **53** 083004
- [12] Shiraki D., Commaux N., Baylor L.R., Cooper C.M., Eidietis N.W., Hollmann E.M., Paz-Soldan C., Combs S.K. and Meitner S.J. 2018 *Nucl. Fusion* **58** 056006
- [13] Bozhenkov S.A. et al 2008 *Plasma Phys. Control. Fusion* **50** 105007
- [14] Chen Z.Y. et al 2013 *Plasma Phys. Control. Fusion* **55** 035007
- [15] Gobbin M. et al 2018 *Plasma Phys. Control. Fusion* **60** 014036
- [16] Ficker O. et al 2019 *Nucl. Fusion* **59** 096036
- [17] Lehnen M., Bozhenkov S.A., Abdullaev S.S. and Jakubowski M.W. 2008 *Phys. Rev. Lett.* **100** 255003
- [18] Finken K.H., Abdullaev S.S., Jakubowski M.W., Jaspers R., Lehnen M. and Zimmermann O. 2006 *Nucl. Fusion* **46** S139–44
- [19] Hollmann E.M. et al 2010 *Phys. Plasmas* **17** 056117
- [20] Yoshino R. and Tokuda S. 2000 *Nucl. Fusion* **40** 1293–309
- [21] Gobbin M., Valisa M., White R.B., Cester D., Marrelli L., Nocente M., Piovesan P., Stevanato L., Puiatti M.E. and Zuin M. 2017 *Nucl. Fusion* **57** 016014
- [22] Munaretto S., Chapman B.E., Nornberg M.D., Boguski J., DuBois A.M., Almagri A.F. and Sarff J.S. 2016 *Phys. Plasmas* **23** 056104
- [23] Papp G., Drevlak M., Fulop T., Helander P. and Pokol G.I. 2011 *Plasma Phys. Control. Fusion* **53** 095004
- [24] Papp G., Drevlak M., Fulop T. and Pokol G.I. 2012 *Plasma Phys. Control. Fusion* **54** 125008
- [25] Papp G., Drevlak M., Pokol G.I. and Fulop T. 2015 *J. Plasma Phys.* **81** 475810503
- [26] Liu Y.Q., Parks P.B., Paz-Soldan C., Kim C. and Lao L.L. 2019 *Nucl. Fusion* **59** 126021
- [27] Dexter R.N., Kerst D.W., Lovell T.W., Prager S.C. and Sprott J.C. 1991 *Fusion Technol.* **19** 131
- [28] Sovinec C.R. et al 2004 *J. Comput. Phys.* **195** 355
- [29] Holly D.J. et al 2011 *IEEE/NPSS 24th Symp. on Fusion Engineering* 1–4
- [30] Munaretto S., Chapman B.E., Holly D.J., Nornberg M.D., Norval R.J., Den Hartog D.J., Goetz J.A. and McCollam K.J. 2015 *Plasma Phys. Control. Fusion* **57** 104004
- [31] DuBois A.M., Lee J.D. and Almagri A.F. 2015 *Rev. Sci. Instrum.* **86** 073512
- [32] O'Connell R., Den Hartog D.J., Forest C.B. and Harvey R. 2003 *Rev. Sci. Instrum.* **74** 2001
- [33] Clayton D.J., Almagri A.F., Burke D.R., Forest C.B., Goetz J.A., Kaufman M.C. and O'Connell R. 2010 *Rev. Sci. Instrum.* **81** 10E308
- [34] Anderson J.K., Forest C.B., Biewer T.M., Sarff J.S. and Wright J.C. 2004 *Nucl. Fusion* **44** 162
- [35] Deng B.H., Brower D.L., Ding W.X., Wyman M.D., Chapman B.E. and Sarff J.S. 2006 *Rev. Sci. Instrum.* **77** 10F108
- [36] Connor J.W. and Hastie R.J. 1975 *Nucl. Fusion* **15** 415
- [37] Granetz R.S. et al 2014 *Phys. Plasmas* **21** 072506
- [38] Paz-Soldan C. et al 2014 *Phys. Plasmas* **21** 022514
- [39] Granetz R.S. et al 2014 *Proc. 25th Int. Conf. on Fusion Energy (Saint Petersburg, Russia, 13–18 October 2014)* (Vienna: IAEA) EX/5-1 ([http://www.naweb.iaea.org/naweb/physics/FEC/FEC2014/fec2014-preprints/549\\_EX51.pdf](http://www.naweb.iaea.org/naweb/physics/FEC/FEC2014/fec2014-preprints/549_EX51.pdf))
- [40] Paz-Soldan C., La Haye R.J., Shiraki D., Buttery R.J., Eidietis N.W., Hollmann E.M., Moyer R.A., Boom J.E., Chapman I.T. and JET Contributors 2016 *Nucl. Fusion* **56** 056010
- [41] Paz-Soldan C. 2018 Private communication
- [42] Chen Z.Y. et al 2016 *Nucl. Fusion* **56** 074001
- [43] Fridstrom R. 2018 Private communication
- [44] DuBois A.M., Almagri A.F., Anderson J.K., Den Hartog D.J., Lee J.D. and Sarff J.S. 2017 *Phys. Rev. Lett.* **118** 075001
- [45] DuBois A.M., Scherer A., Almagri A.F., Anderson J.K., Pandya M.D. and Sarff J.S. 2018 *Phys. Plasmas* **25** 55705
- [46] Howell E.C. and Sovinec C.R. 2014 *Comput. Phys. Commun.* **185** 1415
- [47] Fridstrom R., Munaretto S., Frassinetti L., Chapman B.E., Brunzell P.R. and Sarff J.S. 2016 *Phys. Plasmas* **23** 062504
- [48] Izzo V.A. et al 2011 *Nucl. Fusion* **51** 063032